Journal of the Ceramic Society of Japan 126 [8] 662-666 2018
DOI http://doi.org/10.2109/jcersj2.18037

JCS-Japan

FULL PAPER

Synthesis of core-sheath structured fibers of SnO_2/carbon composites by electrospinning

Yuki MAKINOSE[1,‡], Daisuke ASAKURA[1], Hirofumi MATSUDA[1] and Eiji HOSONO[1,†]

[1]Research Institute for Energy Conservation, National Institute of Advanced Industrial Science and Technology, 1–1–1 Umezono, Tsukuba, Ibaraki 305–8568, Japan

Nanostructured SnO_2 is a candidate anode material for lithium ion batteries because of its relaxation of the large volume change accompanying lithium insertion/extraction. Additionally, SnO_2 is a relatively low-cost and high-capacity material. Carbon composite materials with high electroconductivity are suitable for high power performances. In this study, core-sheath structured fiber materials constructed of a vapor grown carbon fiber-core and a composite sheath of poly-crystalline SnO_2/amorphous carbon are fabricated by electrospinning. This electrospinning method is a useful technique for obtaining nanostructured composite fiber materials.

Key-words : SnO_2, Nanowires, Electrospinning, Core-sheath structure

[Received March 3, 2018; Accepted May 21, 2018]

1. Introduction

Recently, lithium ion batteries with high-energy density and high-power properties have attracted attention as secondary batteries for electric vehicles and plug-in hybrid electric vehicles. Among the many research and development issues, such as selection of cathode materials, anode materials, electrolytes, and separators, lithium-alloy-based materials have received considerable attention as anode materials with a high energy density. Tin metal, which is a lithium-alloy based material, exhibits a high theoretical capacity of 990 mAh g^{-1}, owing to the Li–Sn alloying-dealloying reaction, which is higher than that of graphite (372 mAh g^{-1}).[1),2)] However, the reaction is associated with a large volume change (as high as 300%) giving rise to a considerable deterioration of capacity during charge–discharge cycles.[3)] Although the conversion reaction [Eq. (1)] from tin to tin oxide reaction is irreversible for bulk SnO_2, SnO_2 nanomaterials have drawn attention as anode materials because the reaction is reversible.[4),5)] SnO_2 nanomaterials exhibit a large capacity based on the conversion reaction [Eq. (1)] and alloying reaction [Eq. (2)].

$$SnO_2 + 4Li^+ + 4e^- \rightarrow Sn + 2Li_2O \quad (1)$$

$$Sn + 4.4Li + 4.4e^- \rightarrow Li_{4.4}Sn \quad (2)$$

In addition, many studies of nanomaterials for lithium ion batteries have reported on the importance of nanostructuring materials because nanomaterials have a short diffusion length for lithium ions.[6)–9)] Furthermore, electroconductivity of the materials can be improved by carbon coating,[10)–12)] mixing with carbon nanotubes[12)] or graphene,[12)–15)] to achieve high-power performances. Nanostructure control is also important for relaxation of the volume change.[6)–9)]

We have studied various nanowire materials synthesized by electrospinning methods for use as cathodes in lithium ion batteries.[16)–19)] Electrospinning methods are powerful techniques to easily obtain highly crystalline one-dimensional materials including poly-crystals,[16)] meso-crystals,[17),18)] and single crystals.[17),19)] Furthermore, the method can easily form core-sheath composite nanowires with a core of vapor grown graphite fiber (VGCF) and active materials/amorphous carbon sheaths.[19),20)] The VGCF core and amorphous carbon sheath play important roles as electro-conductive paths.

SnO_2 is an attractive anode material for lithium ion batteries and many researchers have reported on the fabrication of SnO_2 nanowires by electrospinning methods.[21)–23)] However, there have been few reports of complex nanowire structures, such as core-sheath structures with carbon-nanotube cores and SnO_2 sheaths. For gas sensing, SnO_2/multiwall-carbon-nanotube composite nanofibers have been reported.[24)] In this study, we report a one-dimensional core-sheath structure of composite materials constructed from a sheath of amorphous carbon/SnO_2 nanocrystals and a VGCF-core fabricated by an electrospinning method.

2. Experimental section

2.1 Materials

Nitric acid (HNO_3, Special grade), methanol (CH_3OH, Special grade), polyacrylic acid [PAA, $(C_3H_4O_2)_n$, MW

† Corresponding author: E. Hosono; E-mail: e-hosono@aist.go.jp
‡ Present address: Interdisciplinary Graduate School of Science and Engineering, Shimane University, 1060 Nishikawatsu, Matsue 690–8504, Japan

250,000, Wako 1st grade], tin(II) chloride ($SnCl_2$, 99.9%) were purchased from Wako Pure Chemical. VGCF-H (vapor grown carbon fiber, multiwall carbon nanotubes) were provided by Showa Denko, and in this paper VGCF-H is denoted as VGCF.

2.2 Synthesis method

$SnCl_2$ (0.6 mmol) and PAA (1.0 g) were dissolved into mixed solution of nitric acid (1 mL), deionized water (9 mL), and methanol (10 mL). VGCF (0.2 g) was ultrasonically dispersed into the solution with an ultrasonic homogenizer (VC-750, IEDA trading). The precursor solution with VGCF was poured into a syringe that was in turn connected to a metal needle. A direct current electric field of 28 kV was applied between the needle and an Al foil target, which was heated by a hot-air blower set at 250°C. The as-spun materials were dried overnight in a vacuum at 100°C. The dried materials were separated from the Al foil and heated at 350°C for 12 h in air and then heated at 700°C for 3 h under a 100 mL/min Ar flow. Here, the sample heated at 350°C in air and that at 700°C under an Ar flow are denoted as Air-350 and Ar-700, respectively.

2.3 Characterization

X-ray diffraction (XRD) patterns were measured on a D8 Advance (Bruker AXS) with Cu Kα radiation. Raman spectra were measured by a Raman spectrometer with a NSR-1000DT (JASCO), with excitation at 632.8 nm from a He–Ne laser. The morphology of the sample was observed with a field-emission scanning electron microscope (FE-SEM) and a bright-field transmission electron microscope (bright field TEM) by a Carl Zeiss Supra 35 and a JEOL JEM-2100, respectively.

3. Results and discussion

Figure 1 shows XRD patterns of the sample heated at 350°C in air (Air-350) and that heated at 700°C under an Ar flow (Ar-700). Both XRD patterns agreed with the pattern of SnO_2 (ICDD: 01-070-6995). Although it has been reported that high temperature heating of composite materials of SnO_2/carbon compounds at 700–800°C in an inert gas atmosphere can result in reduction of SnO_2 and the formation of metal Sn,[25),26)] in these experiments metallic Sn was not detected. We confirmed the reduction of SnO_2 at 800°C. Therefore, we selected the temperature of 700°C. In addition, precursor fibers were heated at lower temperature in air to obtain SnO_2. We considered that this process is important to suppress reduction to metal-Sn.

Figure 2 shows thermogravimetric-differential thermal analysis (TG–DTA) curves of as-spun materials (a) and Ar-700 (b). In Fig. 2(a), a strong exothermic peak appears between 300 and 350°C. The heating temperature in the air

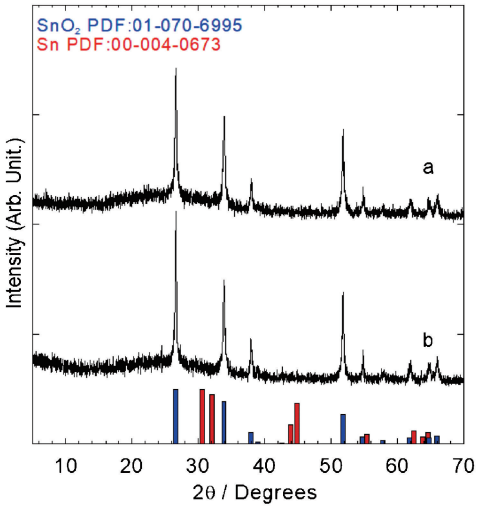

Fig. 1. XRD patterns of SnO_2 nanowires synthesized by electrospinning; (a) Air-350 and (b) Ar-700 under 100 mL/min Ar flow.

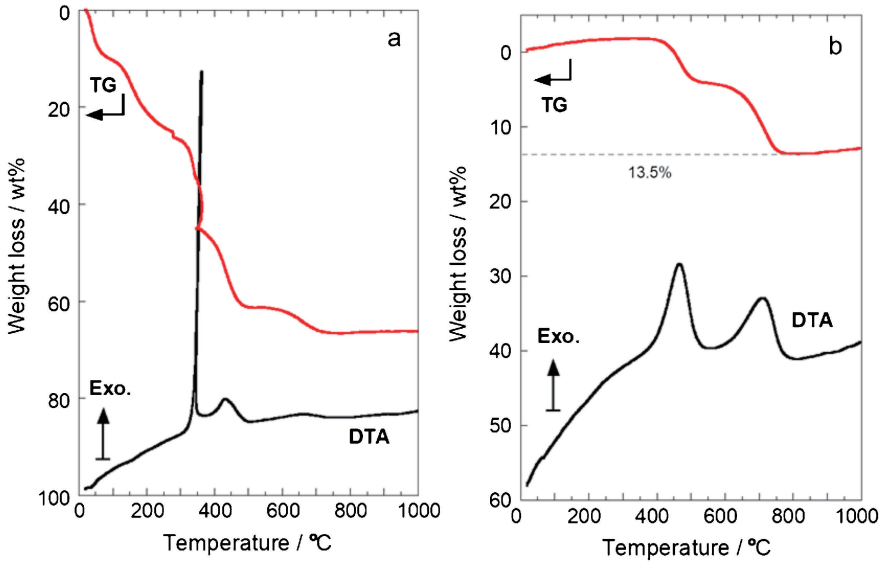

Fig. 2. TG–DTA curves of (a) as-spun material and (b) Ar-700 under 100 mL/min air flow at 5 °C/min heating rate.

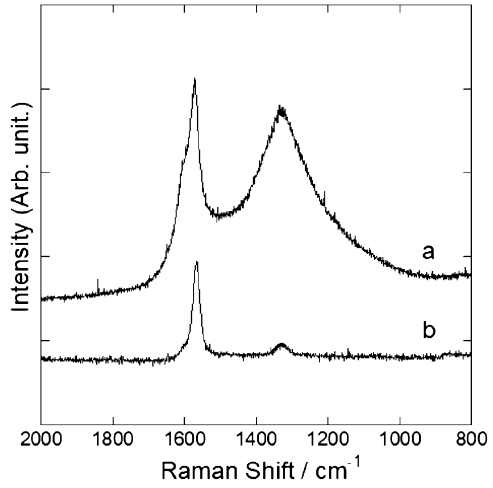

Fig. 3. Raman spectra of (a) Ar-700 and (b) pure VGCF.

conditions of as-spun materials was selected based on the DTA peak. It is considered that formation and crystallization of SnO_2 is occurred at around 350°C because heating of 300°C did not indicate XRD pattern of SnO_2, and TG–DTA curves of polyacrylic acid did not show strong exothermic peak although weight loss was confirmed. The exothermic peak at around 450°C is related to thermal decomposition of polyacrylic acid because TG–DTA curves of polyacrylic acid indicated exothermal reaction at around 400–500°C. In Fig. 2(b), exothermic peaks at around 450 and 700°C are related to decomposition of amorphous carbon (low crystallinity) and VGCF (high crystallinity), respectively. In Fig. 2(b), a weight loss of 13.5 wt% is indicated. We will discuss the weight loss results later.

Figure 3 shows Raman spectra of Ar-700 and pure VGCF. The peaks of D- and G-bands were observed in both spectra at approximately 1350 and ~1590 cm^{-1}, respectively. The spectrum of VGCF showed a sharp peak from a G-band and a weak peak from the D-band owing to the high crystallinity of VGCF, as shown in Fig. 3(b). Conversely, the intensity of the D-band in Ar-700 was greater than that of pure VGCF. In addition, sharp and broad peaks appeared in the region of the G-band, suggesting that the Ar-700 is a composite of amorphous carbon and VGCF.

The XRD and Raman spectra results indicated that Ar-700 is composed of SnO_2, amorphous carbon, and VGCF. Thus, the weight ratio of 13.5 wt% in Fig. 2(b) likely reflects the ratio of carbon materials (including amorphous carbon) and VGCF in the Ar-700. The ratios of D-band/G-band are 0.88 and 0.22 in spectrum of Ar-700 [Fig. 3(a)] and pure VGCF [Fig. 2(b)], respectively. In carbon materials of 13.5 wt%, amorphous carbon is included around 66%.

Figure 4 shows FE-SEM images of the as-spun materials, Air-350 and Ar-700. Figures 4(a) and 4(b) of the as-spun materials shows the fiber morphologies. Furthermore, FE-SEM images in Figs. 4(c) and 4(d) and Figs. 4(e) and 4(f) of Air-350 and Ar-700 also show the fiber morphology, respectively. Thus, the one-dimensional morphology was maintained after heat-treatment in air and Ar.

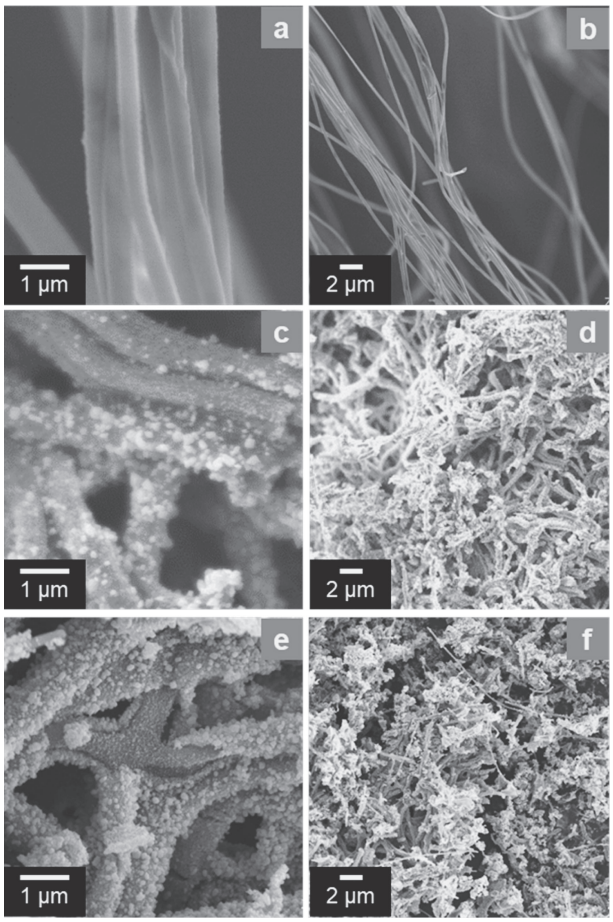

Fig. 4. FE-SEM images of (a, b) as spun nanowire, (c, d) Air-350 and (e, f) Ar-700.

Figure 5, Figs. 5a(a1, a2), 5b(b1, b2) and 5c(c1, c2) show TEM images of Air-350. Figures 5(A) and 5(B) are selected area diffraction patterns (SAED) of the regions A and B in Fig. 5, respectively. The inset images in Figs. 5a(a2), 5b(b2) and 5c(c2) show fast Fourier transform (FFT) patterns of the images. In Fig. 5(A), the SAED pattern is consistent with the pattern of SnO_2. The d-spacing of 4.73 and 3.35 Å reflect the 100 and 110 planes of SnO_2, respectively. Strong spots in the SAED pattern [Fig. 5(B)] and FFT images [Fig. 5a(a2)] are consistent with a d-spacing of ~3.4 Å for VGCF. Thus, the SAED of Figs. 5(A) and 5(B) show that nanoparticles (in region A) and in nanofibers (in region B) of Fig. 5 are SnO_2 and VGCF, respectively. An amorphous phase formed by a pyrolysis reaction of the as-spun materials was observed in Fig. 5c(c2). The Air-350 sample was composed of VGCF, SnO_2 nanoparticles, and an amorphous phase.

Figure 6, Figs. 6a(a1, a2) and 6b(b1, b2) show TEM images and FFT images of Ar-700. The images are similar to those of Air-350 without decomposition of the morphology. In the high magnification images of Figs. 6a(a1, a2) and 6b(b1, b2), a part of the sheath was constructed from SnO_2 nanoparticles and a part was formed by a composite

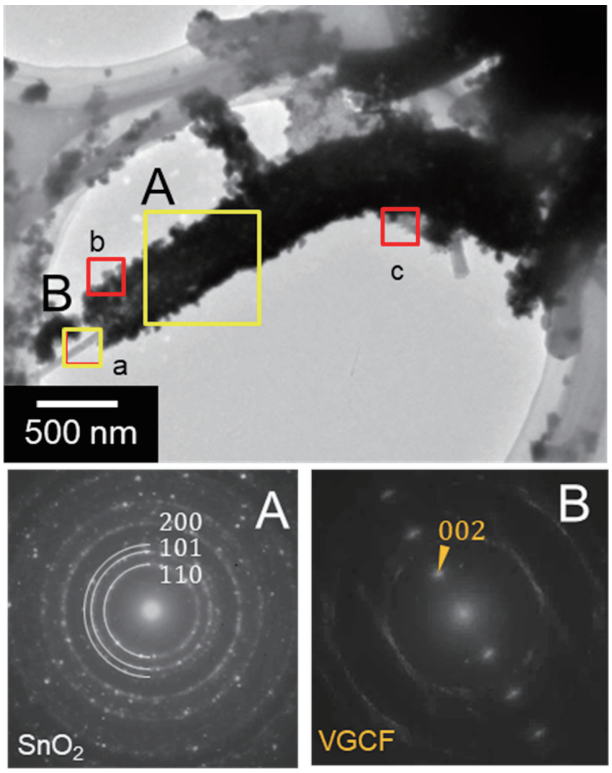

Fig. 5. TEM image and SAED patterns of (A) polycrystalline SnO_2 nanowires and (B) VGCF core of Air-350. Detail of region a, b and c are shown Figs. 5(a)–5(c), respectively.

of amorphous carbon and SnO_2 nanoparticles. Improved crystallinity of some SnO_2 nanoparticles under high temperature heating was indicated by the formation of facets on the SnO_2 crystals. Figure 6a(a2) shows the 101 and $\bar{1}10$ planes of a rutile crystal structure. The amorphous phase in Fig. 6b(b2) was considered to be amorphous carbon based on the Raman spectra results. Thus, electrospinning with a sol–gel solution containing VGCF could be used to easily fabricate core-sheath structured fibers of SnO_2/VGCF/amorphous carbon composite materials.

We evaluated electrochemical performances of SnO_2/carbon composites by measurement of charge–discharge cycle. Although we expected good high-power performances by nanostructure control with carbon materials such as reported papers,[10),27)–30)] the electrochemical performances were not good results. It is considered that high level control of particles size, and optimum composition and constitution by SnO_2, VGCF, and amorphous carbon will improve electrochemical performances. In addition, nanostructure of SnO_2/carbon composite is breakable in the fabrication of slurry. However, electrospinning method is very useful method to complicated nanostructure materials because 1-dimensional materials constructed SnO_2 nanoparticles, VGCF, and amorphous carbon are easily obtained by heating of electrospun fibers. The process does not need mixing process with electroconductive additives after fabricating active materials. We report easy process of complicated 1-dimentional nanostructure materials. This technique will useful for wide variety of applications.

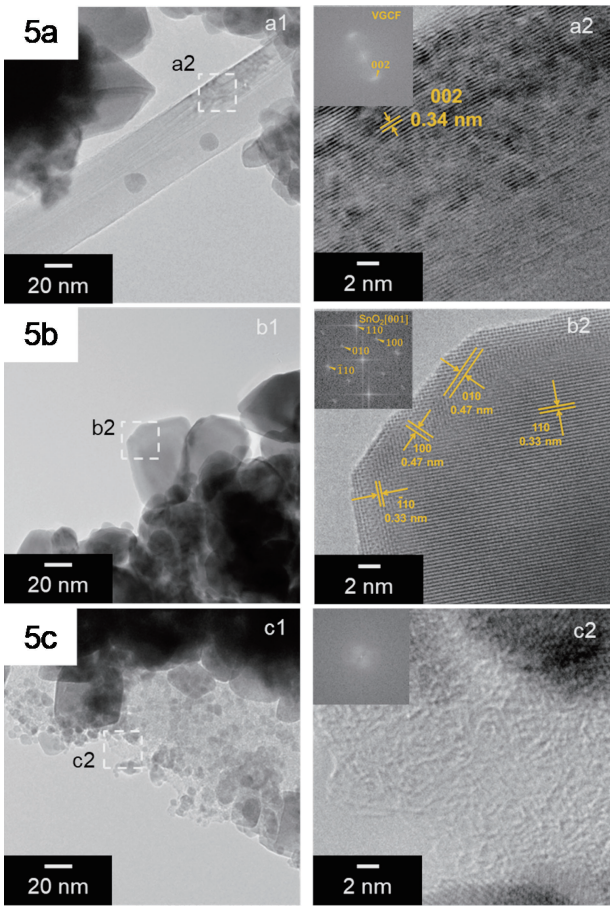

Figure 5a Magnified part of VGCF core of the nanowire in Fig. 5 region a; (a1) low resolution and (a2) high resolution images. The inset image shows fast Fourier transform pattern which was transformed from lattice fringe. Figure 5b Magnified part of SnO_2 nanoparticle of the nanowire in Fig. 5 region b; (b1) low resolution and (b2) high resolution images. The inset image shows fast Fourier transform pattern. Figure 5c Magnified part of amorphous phase of the nanowire in Fig. 5 region c; (c1) low resolution and (c2) high resolution images. The inset image shows fast Fourier transform pattern.

4. Conclusion

Core-sheath fiber materials with a VGCF-core and a composite sheath of SnO_2 and amorphous carbon were synthesized by heat-treatments of as-spun nanowires in air and Ar gas flows. The nanowires were synthesized by electrospinning using VGCF in a mixture containing tin chloride and PAA. Thus, electrospinning is shown to be a convenient process for obtaining composite materials such as core-sheath fibers.

Acknowledgements This work is partially supported by the International joint research program for innovative energy technology by Ministry of Economy, Trade and Industry, Japan. A part of this work was supported by JSPS KAKENHI Grant Number 15K05659. TEM was carried out by the joint research in the Institute for Solid State Physics, the University of Tokyo. We acknowledge Dr. Daisuke Nishio-Hamane to give me some advices about using TEM.

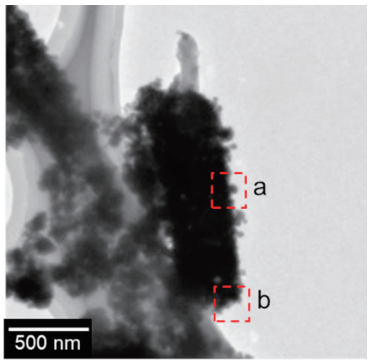

Fig. 6. TEM image of Ar-700. Region a and b show magnified part of Figs. 6(a) and 6(b), respectively.

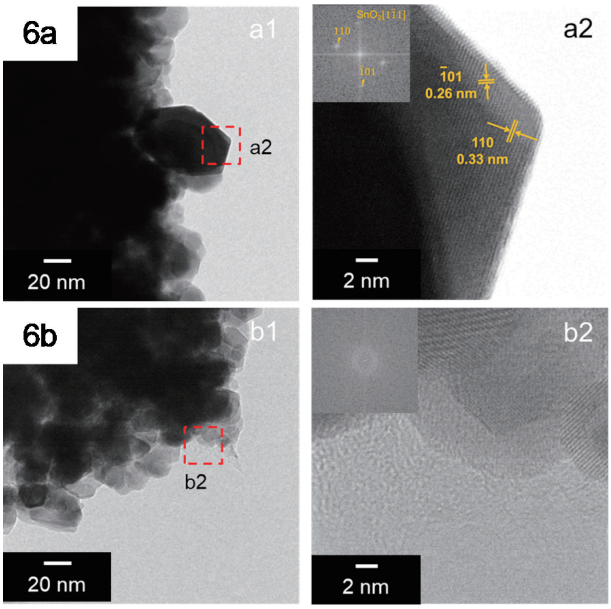

Figure 6a Magnified part of SnO_2 nanoparticle of Ar-700 in Fig. 6 region a; (a1) low resolution and (a2) high resolution images. The inset image shows fast Fourier transform pattern which was transformed from lattice fringe. Figure 6b Magnified part of amorphous phase of Ar-700 in Fig. 6 region b; (b1) low resolution and (b2) high resolution images. The inset image shows fast Fourier transform patterns which was transformed from amorphous phase.

Reference

1) B. Scrosati and J. Garche, *J. Power Sources*, 195, 2419–2430 (2010).
2) N. Nitta and G. Yushin, *Part. Part. Syst. Char.*, 31, 317–336 (2014).
3) N. Li, C. R. Martin and B. Scrosati, *Electrochem Solid St.*, 3, 316–318 (2000).
4) R. Hu, D. Chen, G. Waller, Y. Ouyang, Y. Chen, B. Zhao, B. Rainwater, C. Yang, M. Zhu and M. Liu, *Energy Environ. Sci.*, 9, 595–603 (2016).
5) B. Jiang, Y. He, B. Li, S. Zhao, S. Wang, Y.-B. He and Z. Lin, *Angew. Chem. Int. Edit.*, 56, 1869–1872 (2017).
6) H. T. Tan, X. Rui, W. Sun, Q. Yan and T. M. Lim, *Nanoscale*, 7, 14595–14607 (2015).
7) X. Ma, W. Luo, M. Yan, L. He and L. Mai, *Nano Energy*, 24, 165–188 (2016).
8) J. Graetz, C. C. Ahn, R. Yazami and B. Fultz, *J. Electrochem. Soc.*, 151, A698–A702 (2004).
9) P. Roy and S. K. Srivastava, *J. Mater. Chem. A*, 3, 2454–2484 (2015).
10) Y. Sun, C. Zhao, M. Shen, Z. Pan and X. Liu, *J. Alloy. Compd.*, 683, 191–197 (2016).
11) P. Wu, N. Du, H. Zhang, J. Yu, Y. Qi and D. Yang, *Nanoscale*, 3, 746–750 (2011).
12) J. S. Chen and X. W. D. Lou, *Small*, 9, 1877–1893 (2013).
13) X. Zhou, L.-J. Wan and Y.-G. Guo, *Adv. Mater.*, 25, 2152–2157 (2013).
14) J. Lin, Z. Peng, C. Xiang, G. Ruan, Z. Yan, D. Natelson and J. M. Tour, *ACS Nano*, 7, 6001–6006 (2013).
15) S. Paek, E. Yoo and I. Honma, *Nano Lett.*, 9, 72–75 (2009).
16) Y. Mizuno, E. Hosono, T. Saito, M. Okubo, D. Nishio-Hamane, K. Oh-ishi, T. Kudo and H. Zhou, *J. Phys. Chem. C*, 116, 10774–10780 (2012).
17) S. Kajiyama, J. Kikkawa, J. Hoshino, M. Okubo and E. Hosono, *Chem.- Eur. J.*, 20, 12636–12640 (2014).
18) J. Kikkawa, E. Hosono, M. Okubo, K. Kagesawa, H. Zhou, T. Nagai and K. Kimoto, *J. Phys. Chem. C*, 118, 7678–7682 (2014).
19) K. Kagesawa, E. Hosono, M. Okubo, J. Kikkawa, D. Nishio-Hamane, T. Kudo and H. Zhou, *CrystEngComm*, 15, 6638–6640 (2013).
20) K. Kagesawa, E. Hosono, M. Okubo, D. Nishio-Hamane, T. Kudo and H. Zhou, *J. Power Sources*, 248, 615–620 (2014).
21) L. Li, X. Yin, S. Liu, Y. Wang, L. Chen and T. Wang, *Electrochem. Commun.*, 12, 1383–1386 (2010).
22) D. Kim, D. Lee, J. Kim and J. Moon, *ACS Appl. Mater. Interfaces*, 4, 5408–5415 (2012).
23) E. S. Pampal, E. Stojanovska, B. Simon and A. Kilic, *J. Power Sources*, 300, 199–215 (2015).
24) A. Yang, X. Tao, R. Wang, S. Lee and C. Surya, *Appl. Phys. Lett.*, 91, 133110 (2007).
25) H. Wang, X. Lu, L. Li, B. Li, D. Cao, Q. Wu, Z. Li, G. Yang, B. Guo and C. Niu, *Nanoscale*, 8, 7595–7603 (2016).
26) R. Liu, W. Su, P. He, C. Shen, C. Zhang, F. Su and C.-A. Wang, *J. Alloy. Compd.*, 688, 908–913 (2016).
27) Q. Han, Z. Yi, F. Wang, Y. Wu and L. Wang, *J. Alloy. Compd.*, 709, 227–233 (2017).
28) J. Qu, Y. Yang, X. Shi, W. Wang, J. Ding, N. Yuan, X. Zhao and C. Lai, *J. Alloy. Compd.*, 686, 122–129 (2016).
29) X. Lu, H. Wang, Z. Wang, Y. Jiang, D. Cao and G. Yang, *J. Alloy. Compd.*, 680, 109–115 (2016).
30) J. Liang, J. Wang, M. Zhou, Y. Li, X. Wang and K. Yu, *J. Alloy. Compd.*, 673, 144–148 (2016).